Engineering Structures 296 (2023) 116965

Contents lists available at ScienceDirect

Engineering Structures

journal homepage: www.elsevier.com/locate/engstruct

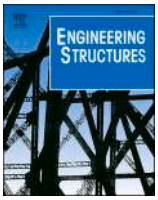

Cyclic tests on two-leaf rubble stone masonry spandrels strengthened with CRM coating on one or both sides

N. Gattesco [a], I. Boem [a,*], E. Rizzi [a], A. Dudine [b], M. Gams [c]

[a] Department of Engineering and Architecture, University of Trieste, Via Alfonso Valerio 6/1, 34127 Trieste, Italy
[b] Fibre Net S.p.a., Via Jacopo Stellini, 3 – Z.I.U., 33050 Pavia di Udine, UD, Italy
[c] Faculty of Civil and Geodetic Engineering, University of Ljubljana, Jamova cesta 2, 1000 Ljubljana, Slovenia

ARTICLE INFO

Keywords:
Composites
Glass fibres
Structural strengthening
Two-leaf stone masonry
Masonry spandrels
Composite Reinforced Mortar

ABSTRACT

The paper reports the results of an original experimental campaign carried out on full-scale, two-leaf rubble stone masonry spandrels retrofitted using the Composites Reinforced Mortar (CRM) technique, applied on one or both wall faces. The CRM system consisted of a mortar coating reinforced with Glass Fibre-Reinforced Polymer (GFRP) meshes and GFRP transverse connectors to promote the connection with the existing masonry. When the coating was applied on one side, additional transverse connectors, made of grout cores with embedded steel ties (artificial diatons), were also used. These elements further strengthened the connection between the coating and the masonry and connected the leaves of the multi-leaf stone masonry walls.

The GFRP mesh in the mortar coating provided the walls with the capacity to resist tension: once the coating and the masonry cracked, the strengthened samples withstood higher distortions, exhibited increased ductility and developed very diffuse crack patterns before collapsing, yielding greater energy dissipation. Furthermore, the transverse connectors enabled the composite action of the CRM coating and the walls and, in the case of artificial diatons, prevented the separation of the masonry leaves.

The resistance of the walls with the CRM coating on one and both sides was 2.8 and 3.4 times that of the plain samples, respectively; in both cases, the ultimate drift was more than five times larger than the reference, while the cumulative dissipated energy was more than 30 times. The equivalent hysteretic damping in the damaged state was 11–14% (for CRM on one side) and 8–9% (for both sides).

1. Introduction

Past and recent earthquakes worldwide have shown the high vulnerability of historical masonry buildings, particularly those made of stones with irregular textures, poor-quality mortar, and traditional wooden floors [1–3]. Consistently, the European Macro-seismic Scale EMS-98 [4] identified filed stone and coursed rubble masonry buildings among the most seismically vulnerable structures. Because of the weak connections between the walls and the negligible diaphragm action provided by the floors, these massive, non-engineered constructions frequently lack integrity, resulting in the disaggregation or separation of wall leaves [5]. The design of proper strengthening strategies for such structures is both urgent and challenging. The compatibility between the new materials and the old masonry and proper detailing of the interventions are essential to avoid ineffectiveness (e.g., glueing composite strips on the masonry surface does not improve the wall's integrity) and worsening the seismic response (e.g., the addition of thick reinforced concrete layers on the walls, of rigid heavy floors or of reinforced concrete (RC) bond beams within the wall) [6,7].

Within this context, the Interreg Italia-Slovenija project "CONSTRAIN" [8] aimed to study innovative strategies for fast and efficient seismic protection of existing masonry buildings using composite fibre–reinforced coatings, floor ties and strengthened bond beams [9]. In particular, this paper focuses on an experimental study for assessing the effectiveness of Composite Reinforced Mortar (CRM) coatings for the retrofitting of double-leaf rubble stone masonry spandrels.

The CRM technique, which consists of the application of mortar coatings with embedded, preformed fibre-based composite meshes and transversal fibre-based composite connectors, is particularly suitable for historical rubble stone masonry because of the chemical and mechanical compatibility of the mortar for coating and masonry (differently, e.g.,

* Corresponding author.
E-mail address: ingrid.boem@dia.units.it (I. Boem).

https://doi.org/10.1016/j.engstruct.2023.116965
Received 21 June 2023; Received in revised form 25 August 2023; Accepted 24 September 2023
Available online 29 September 2023

from non-transpiring and rigid concrete slabs, such as reinforced concrete coatings). In addition, this approach provides good adhesion to such rough surfaces (in contrast, e.g., to glued fibre-based composites, such as Fibre-Reinforced Polymers).

The CRM strengthening systems have been widely investigated through both material characterisation tests and tests on masonry panels under in- and out-of-plane loading conditions [10–16]. CRM-strengthened spandrels, on the other hand, have not been adequately addressed. Because the coupling effect of spandrels influences the transfer and distribution of seismic forces [17] it, thus, needs to be known to perform reliable seismic behaviour predictions of structures. This is even more significant in traditional rubble stone buildings, which typically lack strong floors and ring beams capable of providing this coupling effect.

Three main testing setups were designed in the literature for testing masonry spandrels. The first setup was adopted by both Augenti et al. [18] and Ismail and Ingham [19] and consisted of "TT-shaped" sample panels composed of two piers fixed at the base and loaded with a constant vertical load at the top, coupled with a spandrel. Additionally, a reversed cyclic loading was applied at the top of the samples. The second setup, adopted by Gattesco et al. [20], consisted of an "H-shaped" masonry panel (two lateral pier portions joined by a central spandrel), with piers clamped under a constant axial stress; one pier was fixed at the base while the other was subjected to cyclic up–down lifts. The third setup, proposed by Beyer et al. [21], also concerned "H-shaped" masonry panels with pre-compressed piers, in which the spandrel deformation was accomplished by applying a simultaneous cyclic rotation at the base of the piers.

The tests reported in this paper were carried out according to the latter test setup at the University of Ljubljana (Slovenia). The tests aimed to evaluate and compare the performances of the spandrels before and after applying CRM coatings. Two CRM coating configurations were considered: both wall sides or only one side. The two-sided coating was expected to perform better, having twice the reinforcement, symmetry and, to some extent, masonry confinement provided by the passing-trough transverse connectors. However, in actual applications, designers often need to find lighter, faster and less expensive methods. The most apparent simplification is applying the coating to only one side. Still, in traditional rubble stone structures without connected leaves, which may suffer from disaggregation and leaf separation phenomena, such a solution is not suitable. Thus, the application of CRM coating on one side was combined with the introduction of artificial diatons to achieve the monolithic behaviour of both masonry leaves and the CRM.

The application of one-sided, composite fibre–reinforced mortar coatings has been addressed in the literature (although not on spandrels). For example, in [22] and [23], diagonal compression tests were performed on solid brick and tuff masonry panels strengthened with basalt Textile Reinforced Mortar (TRM) coating without mechanical anchorage. The strength increase exhibited by single-sided reinforced samples was almost half that of double-sided reinforced panels (having half the reinforcement ratio); in addition, no mortar debonding occurred. However, because of the eccentric stiffness, the response of single-sided reinforced samples was affected by out-of-plane bending, which limited the post-peak deformation capacity. Similar conclusions were drawn in [24] for tuff masonry samples strengthened on one side by means of glass Fibre-Reinforced Cementitious Matrix (FRCM); moreover, the introduction of composite anchors improved the response in both strength and ductility. In [25], the solid brick specimens strengthened on one side with glass FRCM bent towards the reinforced side, but this did not result in a ductility reduction; instead, the mortar coating debonded. Furthermore, the different glass fibre–reinforced CRM systems applied in [15] on one side of tuff masonry panels provided a greater deformation capacity than that of the double-sided strengthened samples since the mortar debonding affected only the latter set.

General conclusions from the literature are difficult to draw: the effect of single-sided applications compared with double-sided ones appear to be strictly related to the mechanical and geometrical properties of the strengthening system. Additionally, the observations are based on simplified tests in terms of load pattern and boundary conditions, which do not represent the actual conditions. Lastly, multiple-leaf or irregular masonry is not considered, although they are more likely to have drawbacks due to single-side strengthening. For example, in [26] and [27], debonding of the CRM coating and masonry leaf separation occurred in rubble stone masonry piers subjected to shear-compression tests because the transversal anchors were too weak.

The present work aims to provide original results on spandrels tested in the representative loads and boundary conditions in the laboratory. Furthermore, the highly vulnerable double-leaf rubble stone masonry typology is considered. The main features of the samples and the testing apparatus are reported in the following section; then, the test results are described in terms of capacity curves and damage pattern evolution. Finally, the results are analysed and compared, providing useful information on the effectiveness of the CRM coating in terms of resistance, displacement, stiffness and dissipative capacities.

2. Materials

2.1. Samples characteristics

First, two identical masonry samples were built and tested in the reference unstrengthened state (id. S-R2-U1 and S-R2-U2) up to a damage level near the ultimate limit. Then, the samples were strengthened – the former with coating on one side (id. S-R2-R1) and the latter on both sides (id. S-R2-R2) – and retested to near collapse. The experimental samples were H-shaped walls (Fig. 1), 350 mm thick, and composed of a masonry beam (1050 × 1000 mm^2, width × height) joining two external masonry pier portions (1420 × 2190 mm^2, width × height). A timber lintel (350 × 170 mm^2 cross-section), indenting each pier by 150 mm, was introduced under the masonry beam to reproduce a typical arrangement of a historical stone building.

The 350 mm–thick masonry was made of stone units arranged with a weak lime-based mortar in a two-leaf masonry configuration without any connection stone. This type of masonry is typical of traditional stone masonry buildings, which are very common, among others, in the territories of Northern Italy, Slovenia and Northern Croatia. These buildings, mainly two/three storeys, have unidirectional timber floors (timber joists with nailed planks) and walls with thickness usually ranging from 350 mm to 400 mm. Normally, masonry is made of two unconnected leafs (i.e. without header stones) with negligible thickness of the infill. The absence of headers, the low mechanical interlocking and poor bond between the leaves make such buildings particularly vulnerable to seismic actions, since the two leaves tend to separate [28]. Therefore, special attention was paid during the construction to reproduce the discontinuity of leaves. The units were a mix of two Credaro stones, Berrettino and Medolo, with approximate compressive strengths of 170 and 150 MPa, respectively. These stones are of the sandstone type with a calcareous composition. In particular, Berrettino is a rock made of minute detrital grains, mainly carbonate (calcarenite), with evident stratification levels and yellow–brown or pink in colour. In contrast, Medolo is a rock almost entirely of microcrystalline calcium carbonate (crystalline limestone) with a very fine grain size and a hazelnut-grey in colour with light to dark tones. These stones were selected as representative, in terms of lithological and mechanical characteristics, of the sandstones typically used in Northern Italy and Slovenia stone buildings. Such elements are particularly resistant and rigid, and then the behaviour of the masonry is mostly influenced by the mortar characteristics and the units arrangement.

The masonry mortar was carefully designed with a granulometric distribution similar to those found in historic masonry buildings [29] with a hydraulic lime-to-sand ratio of 1:7 by mass (i.e., 200 kg hydraulic lime and 1400 kg of sand per m^3 of mortar). The distribution of the

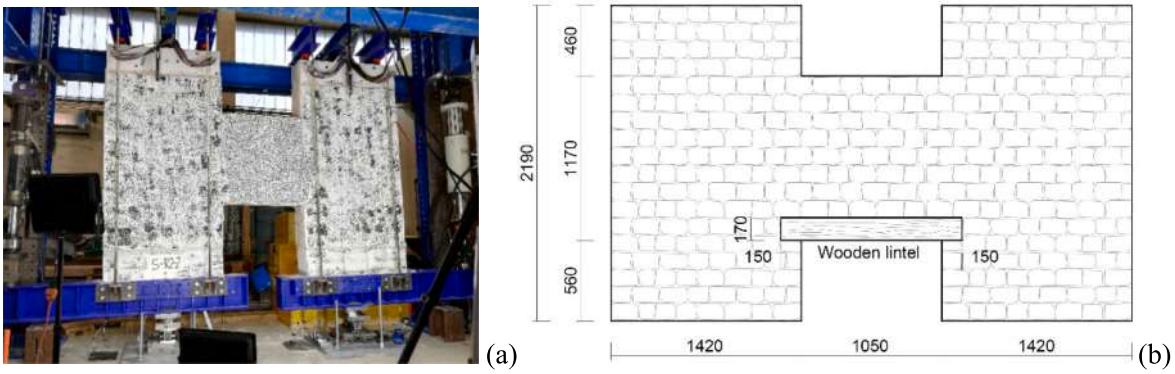

Fig. 1. Spandrel samples: (a) global view of the experimental setup and (b) main geometric characteristics (dimensions in mm).

Table 1
Mechanical properties of the masonry mortar with respective coefficients of variation (CoV).

Sample	Number of tests	Property of masonry mortar	Mean value [MPa]	CoV [%]
S-R2-U1	30	Flexural tensile strength	0.22	12.7
		Compressive strength	1.10	12.1
S-R2-U2	21	Flexural tensile strength	0.34	28.0
		Compressive strength	1.95	12.0

Table 2
Mechanical properties of the mortar of the coating with coefficient of variation *CoV*.

Sample	Number of tests	Property of mortar coating	Mean value [MPa]	CoV [%]
S-R2-R1	4	Flexural tensile strength	4.17	5.2
		Compressive strength	22.93	10.0
S-R2-R2	12	Flexural tensile strength	5.64	4.1
		Compressive strength	24.55	5.3

aggregate ranged between 0.05 and 3 mm, and about 45 % of the sand grains were smaller than 0.5 mm. The mortar was sampled during the construction and tested after air curing to determine the flexural and compressive strengths [30]; the main results are summarised in Table 1.

To estimate the main mechanical characteristics, compressive tests were carried out on two masonry wallets having a width of 500 mm and a height of 1010 mm. The tests were performed accordingly to EN 1052–1 [31]. The sample was placed on the laboratory's strong floor and compressed by a vertical actuator (1000 kN capacity), equipped with a load cell. A stiff steel profile was placed between the actuator and the wall, so to ensure a uniform stress distribution. Each sample was equipped with four linear potentiometer transducers, two on each side, to measure the vertical shortenings around the mid-height of the sample, on a base length of about 500 mm (stroke 100 mm). The load was applied monotonically and at a constant rate until failure, taking about 30 min to complete the test. The Young's modulus was calculated from the secant of the stress–strain curve at a third of the compressive capacity. From about 45 % of the resistance, vertical cracks formed in the mortar joints, on both the samples frontal and lateral faces; the cracks progressively grew in length and width as the load increased. Close to the peak load, the mortar was crumbling and falling out. The tests yielded an average compressive strength of 2.48 MPa and Young's modulus of 1074.2 MPa.

2.2. Strengthening method

The CRM coatings applied to strengthen the samples had nominal thicknesses of 30 mm, the minimum necessary to ensure an adequate embedding and covering of the fibre-based composite mesh and of the additional connectors within the coating. The mortar of the coating was a natural hydraulic lime compound (specific weight of about 18 kN/m^3). The mortar was regularly sampled and tested after at least one month of air curing [30]. The mechanical properties obtained by testing are summarised in Table 2.

The GFRP mesh embedded within the coating had a 66 × 66 mm^2 grid composed of twisted-fibre wires in the warp direction weaved on parallel-fibre wires in the weft direction (dry fibre cross-sectional area in the wire of 3.8 mm^2). Tensile tests were carried out on the GFRP wires to determine the tensile strength and axial stiffness. The test samples were constituted by single 500 mm long wires extracted from the GFRP mesh by cutting the transversal wires; cardboard tabs pairs were used as clamping heads. Tensile tests were performed according to ISO 10406–1:2015 [32], by testing five test samples for each typology. A testing machine "Galileo" was used; the load was measured by using a pressure transducer (20 kN capacity). A linear extensometer was installed along the axis of the central portion of the test piece, on a base length of 70 mm (stroke 10 mm, error lin. ± 0.10 %). The load was applied at a constant rate (1.0 % strain per minute). The axial stiffness EA_{tot} was calculated from the secant of the load–strain curve at 20 % and 50 % of the tensile capacity. Table 3 summarises the main results.

Table 3
Properties of the GFRP wires: tensile resistance T_w, tensile strength f_w, (referred to the dry fibres cross section, 3.8 mm^2), ultimate strain ε_u and axial stiffness EA_{tot}.

Property	Twisted mesh wires		Parallel mesh wire	
	Mean	CoV [%]	Mean	CoV [%]
T_w (kN)	5.11	2.4	5.93	3.9
f_w (MPa)	1345	–	1561	–
ε_u (%)	1.85	1.9	2.03	4.2
EA_{tot} (kN)	276.7	2.6	291.2	1.6

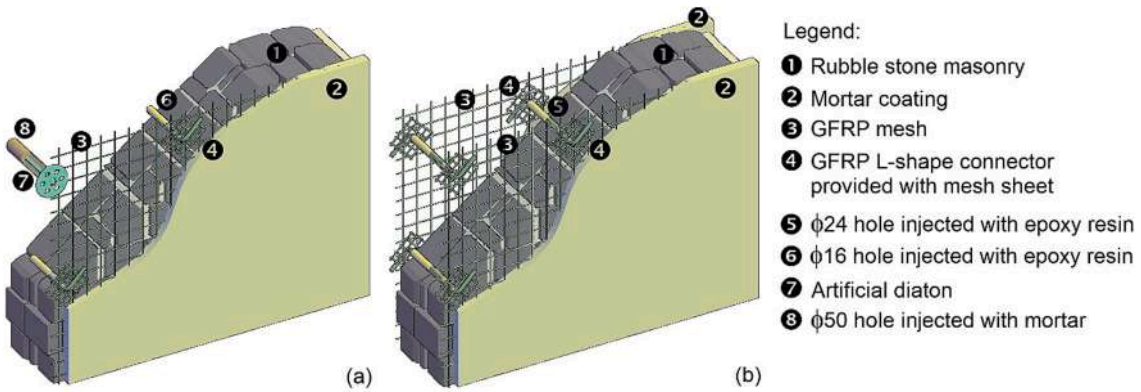

Fig. 2. Details of the retrofitting intervention for application (a) on one or (b) on both sides.

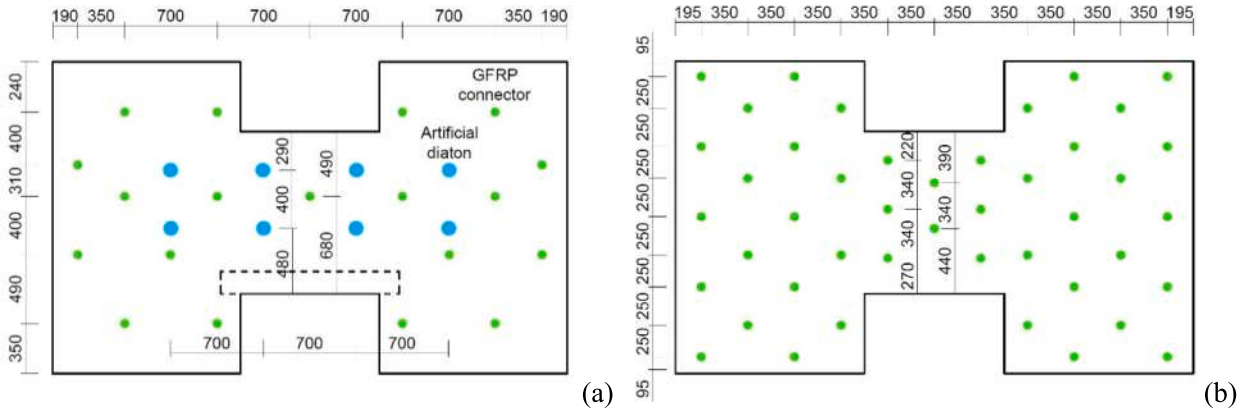

Fig. 3. Positioning of the connectors for (a) S-R2-R1 and (b) S-R2-R2.

For the one-sided CRM coating configuration (Fig. 2a, test S-R2-R1), a combination of GFRP L-shaped connectors (4/m^2) and artificial diatons (eight in the spandrel–pier area) was introduced, according to the arrangement illustrated in Fig. 3a. The GFRP connectors were inserted into 16 mm diameter holes drilled in the masonry 300 mm deep and injected with a vinyl ester epoxy resin. Each connector had a cross-section of 7 × 10 mm^2 and a nominal dry fibre cross-section of 32.4 mm^2; they had a nominal characteristic tensile strength of 17 kN and an ultimate strain of 1.9 %. In front of each connector, a small GFRP mesh sheet with a 33 × 33 mm^2 grid was positioned to distribute stresses within the coating. The artificial diatons were made with a 16 mm diameter threaded, stainless steel bar, 365 mm long, centred in a 50 mm diameter hole and embedded in a high-resistance thixotropic cement-based mortar. The holes were drilled using a water-cooled core drilling machine. The diatons had the critical role of joining the wythes of the masonry and acting as connectors for the CRM coating. To connect the mortar coating to the diatons, perforated stainless steel washers (4 mm thick), with a nut welded at each centre, were screwed onto the

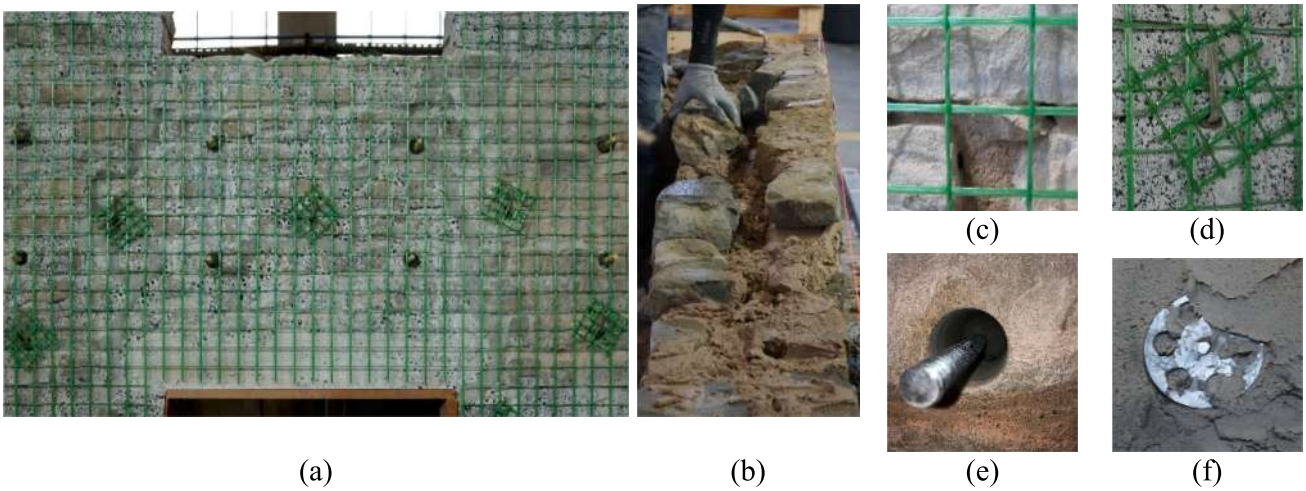

Fig. 4. Details of sample S-R2-R1: (a) global view before applying the mortar coating, showing the repointed cracks from the test in the reference state, and details of (b) two-leaf masonry construction, (c) GFRP mesh, (d) GFRP connector with additional GFRP mesh sheet, (e-f) steel bar and head washer of the artificial diaton.

head of the threaded bar at half the thickness of the CRM coating above the GFRP mesh. The term "artificial diaton" recognises a transversal tying element not originally present in the masonry and introduced during the strengthening intervention. In contrast, "non-artificial diaton" or, simply, "diaton", commonly refers as a large stone element arranged as header during the wall construction, connecting the leaves. Some detail pictures of the strengthening intervention are illustrated in Fig. 4.

In the case of CRM applied to both wall faces (Fig. 2b, test S-R2-R2), the coating was anchored to the walls using pairs of GFRP L-shaped connectors (6/m^2) inserted into 24 mm diameter holes drilled in the masonry, ensuring an overlap of at least 200 mm, and injected with a vinyl ester epoxy resin (Fig. 3b).

Generally, the number, position and diameter of connectors are crucial for the transversal tying and depend on the masonry texture, thickness and mechanical characteristic. In lack of a specific design procedure, was made to the literature. In particular, the GFRP injected connectors were distributed by considering the range 4–6/m^2 suggested by Tomaževič [17] for traditional reinforced-cement coating. Past experimental tests on CRM strengthened walls, with transversal GFRP connectors, proved such amount adequate in case of both in-plane [11] and out-of-plane [12] actions. For dimensioning the artificial diatons, reference was made to the ranges suggested by Castori et al. [28] for historic hard-stone masonry (barely cut stones and pebbles assembled with lime-based mortars): connector diameter: 16–20 mm; hole diameter to connector diameter ratio: 3–4; connectors distance to hole diameter ratio: 9–11. In the experimental samples the artificial diatons were installed in only the spandrel area because their influence, for the test purpose, is negligible in the other portions.

Before applying the CRM coating, the mortar in masonry joints was removed to a depth of 10 mm, and the masonry surface was washed with a high-pressure water cleaner to remove the white hydraulic lime paint and moisten the masonry surface for better adhesion of the CRM coating. White paint was applied on the façade to facilitate the detection of cracks during the test on the unreinforced building. Furthermore, the visible cracks that emerged when testing the unstrengthened configurations were repaired by grouting with cement mortar in the first 10–20 mm of the crack depth.

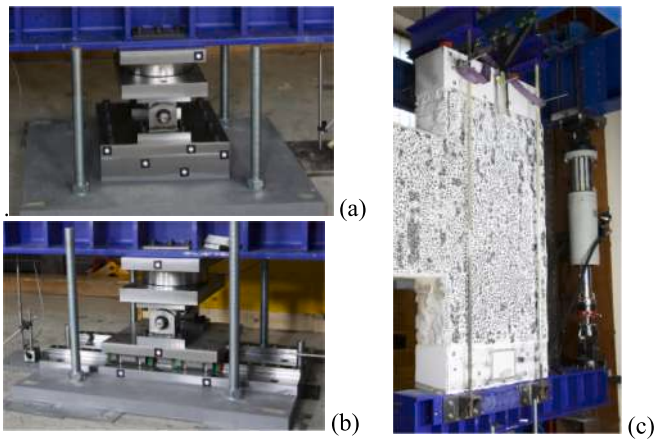

Fig. 6. Details of the testing apparatus: (a) left and (b) right supports and (c) vertical clamping of a pier.

3. Methods

3.1. Loading layout

The test setup was basically designed to apply equal rotations at the base of the two piers. In detail, the test apparatus, illustrated in Fig. 1a and schematised in Fig. 5, consisted of two independent 3000 mm long stiff steel beams (HEB 400 "lever beams"), arranged horizontally. The support of the left lever beam allowed only rotation (Fig. 6a), while the right one allowed rotation and sliding (Fig. 6b); both supports could withstand tension and compression. The free horizontal sliding of the right support was permitted so that the tests detect specifically the coupling effect of the spandrel within the two piers due to mechanisms not influenced by the horizontal piers constrain. On the contrary, with

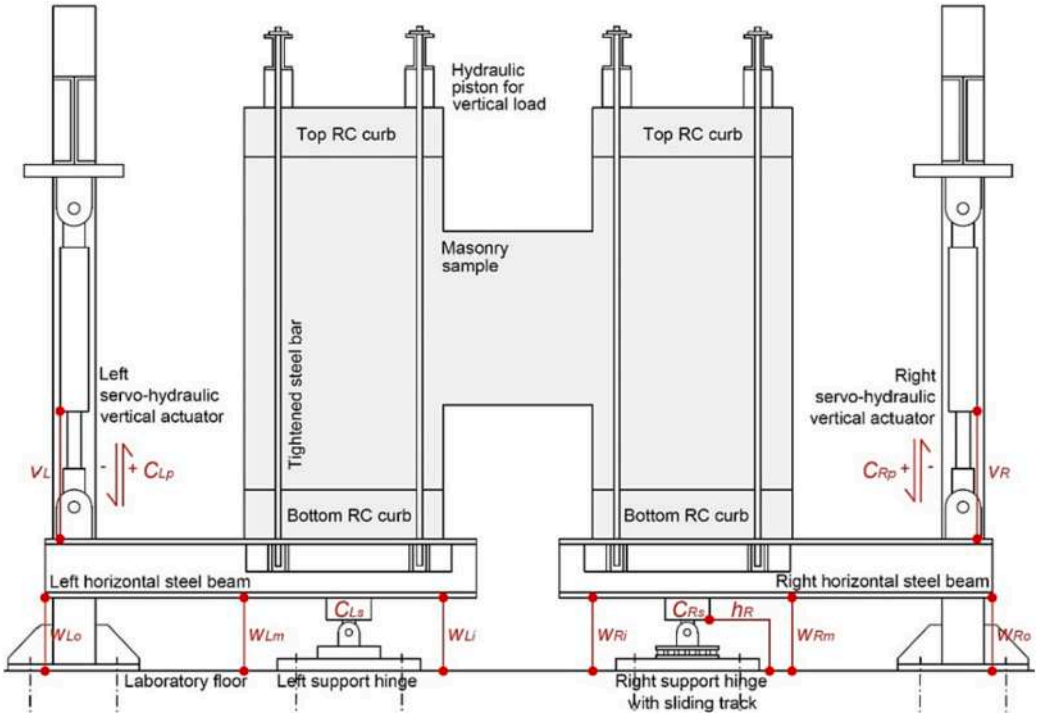

Fig. 5. Schematisation of the experimental setup.

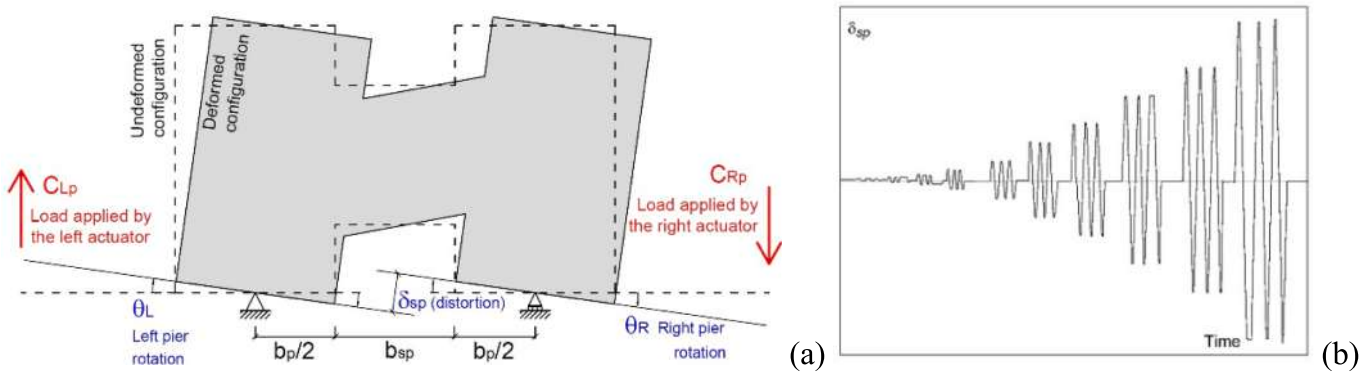

Fig. 7. Evaluation of the spandrel distortion (a) and schematisation of the cycling loading protocol (b).

horizontal sliding restricted, some tying effect would reasonably increase the sample performances restraining the extremities of the diagonal strut forming in the spandrel.

To apply the pier base rotation, each steel beam was connected at the outer extremity to a servo-hydraulic actuator (250 kN capacity, 200 mm stroke) installed vertically above the beam on an independent steel portal frame. The masonry samples were built directly on the apparatus to avoid accidental damage during handling. They were positioned so that each pier lay on a lever beam, and the beam supports were located at the mid-width of the pier. At the base and the top of each pier, reinforced concrete (RC) curbs were introduced (350 × 350 mm^2). To reproduce typical axial stress in the masonry piers in actual buildings, each pier was clamped between the lower lever beam and steel profiles placed at the top (pairs of HEB 400 s), connected by four Dywidag threaded steel bars (24 mm diameter), as shown in Fig. 6c. The application of the axial stress was performed using two pairs of hydraulic actuators (500 kN capacity each), located below the top steel profiles and connected in parallel. The global load applied by these four jacks was maintained constant while the other two actuators (at the ends of the lever beams) moved vertically with the same velocity but in opposite directions. As a result, both piers rotated in the same direction, inducing shear and bending in the spandrel (Fig. 7a).

3.2. Instrumentation

The instrumentation, schematised in Fig. 5, comprised nine potentiometer transducers, four load cells, one pressure transducer and a camera system for the digital image correlation (DIC) measurements. The displacement transducers measured the vertical displacements at the intrados of the left (w_{Lo}, w_{Lm}, w_{Li}) and right (w_{Li}, w_{Lm}, w_{Lo}) lever beams, the horizontal sliding of the right support (h_R) and the elongation of the outer actuators (v_L, v_R). The load cells registered the vertical forces applied by the actuators (C_{Lp}, C_{Rp}) and the vertical reaction at the supports (C_{Ls}, C_{Rs}). The pressure transducer measured the global axial load applied on the piers with the four jacks at the top.

The DIC system method was used to record the complete deformation field on the front surface, registering the sequence of crack formation [33,34]; this allowed the detection of cracks in very early stages, when the damage could not be observed by the naked eye. Before the tests, the surfaces were painted with white paint comprising water and hydraulic lime powder. Then, a random black speckle pattern was applied so the software could detect the surface. Two high-resolution cameras were used to take the photos.

3.3. Test protocol

The tests started by applying the vertical load to the piers (global vertical load of 328 kN, corresponding to a mean compressive stress of 0.33 MPa). Then, the actuators of the two outer jacks, governed through computer software, were moved vertically in opposite directions so that the two lever beams had the same rotation θ, evaluated in accordance with Eq. (1):

$$\theta = \frac{(w_{Lm} + w_{Li})}{b_p} = \frac{(w_{Rm} + w_{Ri})}{b_p} \quad (1)$$

where w_i and w_m are the vertical displacements at the inner and outer corners of the piers, measured at the intrados of the left (L) and right (R) lever beams (Fig. 5), respectively, and b_p is the pier width. The vertical distortion δ_{sp} applied to the spandrel (Fig. 7a) was estimated using Eq. (2):

$$\delta_{sp} = \theta \cdot (b_p + b_{sp}) \quad (2)$$

where b_{sp} is the spandrel width.

Each loading cycle was performed three times in the positive (clockwise rotation of the lever beams) and in the negative (anticlockwise) directions, according to the test protocol shown in Fig. 7b. In the initial cycles, the distortion was increased by small amplitudes, so that the initial damage and stiffness could be evaluated more accurately. After reaching the peak resistance, the amplitude gradually increased as the damage became significant for larger deformations.

Considering the balance of vertical forces, the shear force acting on the spandrel was given by the sum of the load transmitted by the outer actuator and the vertical reaction at the support on the left (or right) lever beam. The mean value between both sides was considered, according to Eq. (3):

$$V_{sp} = \frac{V_{Lsp} + V_{Rsp}}{2} = \frac{(C_{Lp} + C_{Ls}) + (C_{Rp} + C_{Rs})}{2} \quad (3)$$

Values of V_{Lsp} and V_{Rsp} did not differ by more than 3 %.

The specimens were first tested in the unreinforced state up to significant damage. They were then repaired, retrofitted and tested until collapse. This approach allowed for the comparison and estimation of the effectiveness of the strengthening.

4. Results

The spandrel performances are expressed in capacity curves representing the shear load V_{sp} (Eq. 3) with varying distortion δ_{sp} (Eq. 2). The

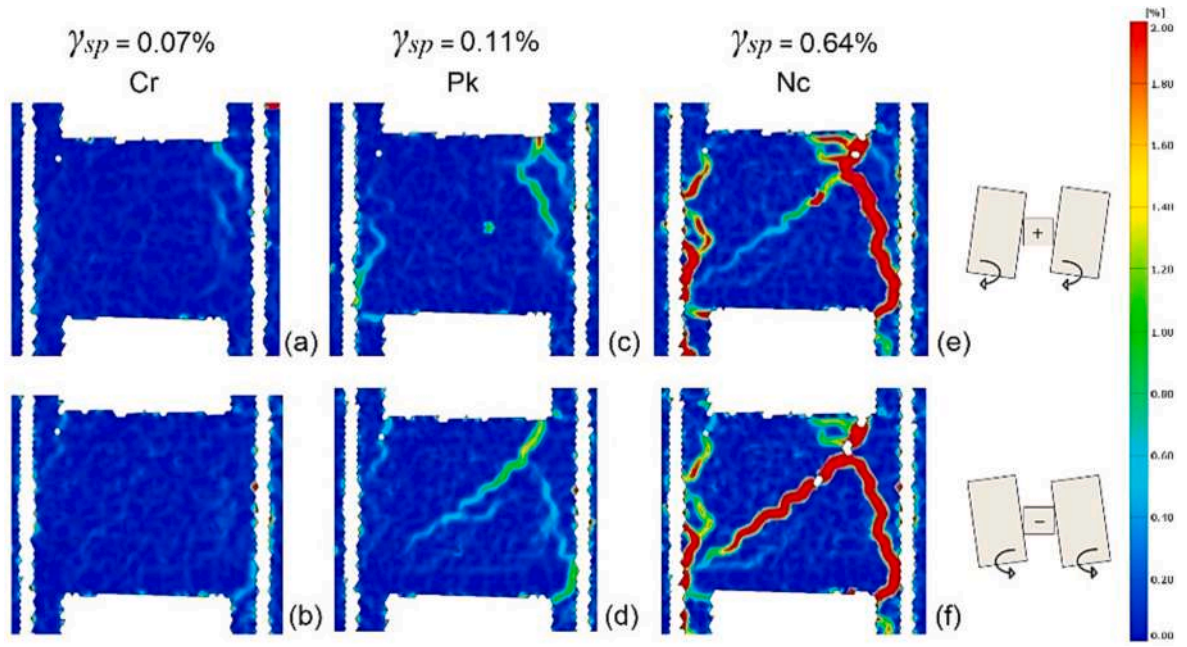

Fig. 8. Evolution of crack pattern in test S-R2-U1, spandrel front face (gradient colour scale represents tensile strain in the range of 0–2%).

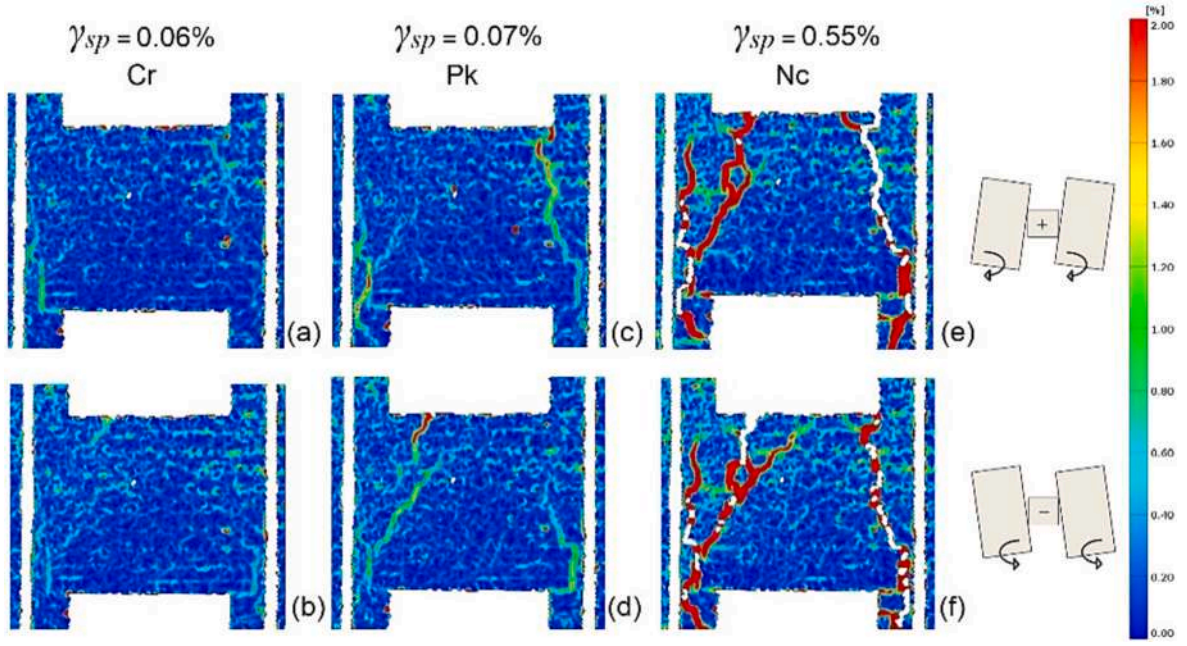

Fig. 9. Evolution of crack pattern in test S-R2-U2, spandrel front face (gradient colour scale represents the tensile strains in the range of 0–2%).

spandrel drift γ_{sp} was determined by dividing δ_{sp} by the spandrel's width of 1050 mm. The behaviours of the four samples are described in the following subsections in terms of capacity curves and damage evolution. The damage evolution is reported as a sequence of pictures captured by the DIC system at first cracking (*Cr*), peak load (*Pk*) and near collapse (*Nc*). The *Nc* state was identified at a 30 % decrease from the peak load.

According to the typical failure mechanisms of historic masonry elements, two groups of cracks were generally distinguished: mainly vertical cracks at the spandrels ends, related to in-plane bending failure, and diagonal cracks within the spandrels, indicative of an in-plane shear mechanism.

4.1. Response of unreinforced samples

The age of the samples at testing was about 40 days. The evolution of the spandrel crack patterns is shown in Figs. 8 and 9; the experimental capacity curves, V_{sp}–δ_{sp}, are illustrated in Figs. 10a and 11a.

In test S-R2-U1, the first cracking occurred at $\delta_{sp} = +0.58$ mm ($V_{sp} = +23.3$ kN) at the top-right corner of the spandrel and, immediately after, at the bottom-left corner (the crack surrounded the end of the timber lintel), as illustrated in Fig. 8a. As the load reversed, these cracks closed, and opposite cracks opened at the top-left and bottom-right corners ($\delta_{sp} = -0.82$ mm, $V_{sp} = -24.0$ kN), as shown in Fig. 8b. With the pier rotations increasing, the cracks at the spandrel ends gradually grew, following the mortar joints with an almost vertical trend, until they

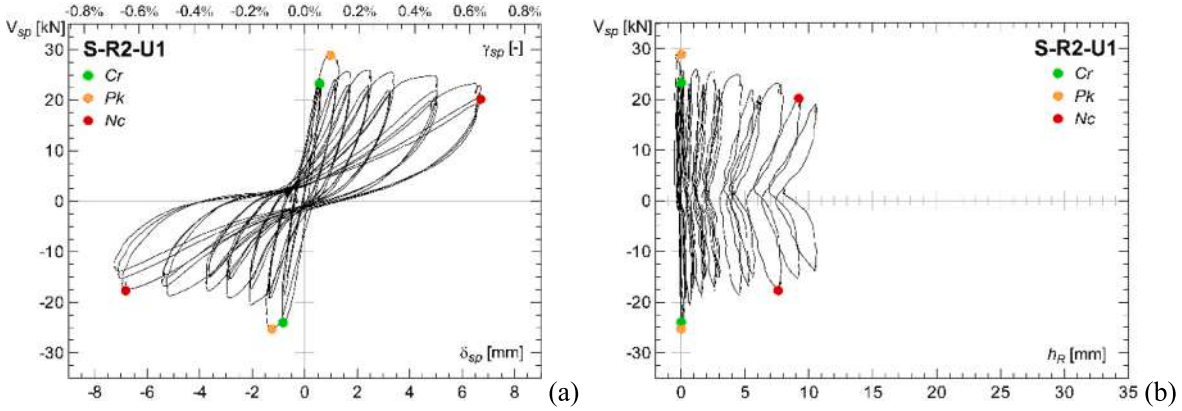

Fig. 10. Test S-R2-U1: (a) V_{sp}–δ_{sp} (or V_{sp}–γ_{sp}) and (b) V_{sp}–h_h curves.

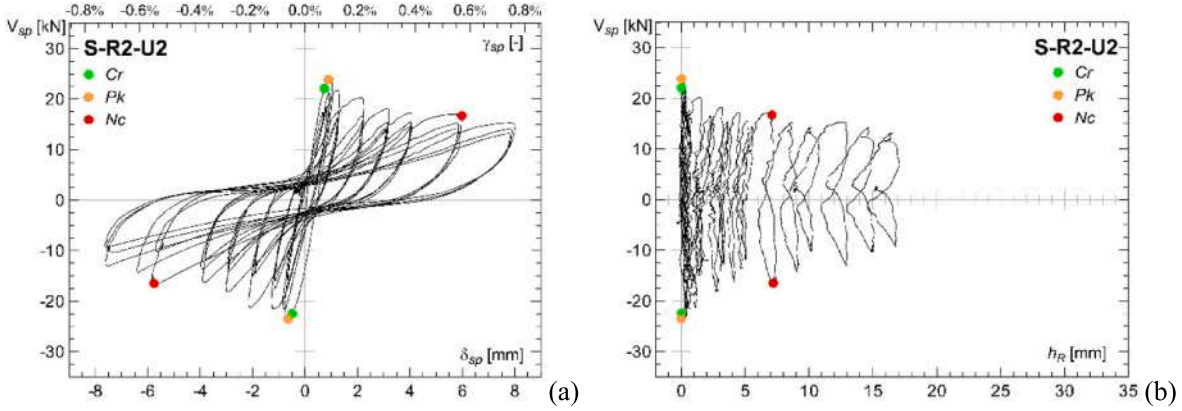

Fig. 11. Test S-R2-U2: (a) V_{sp}–δ_{sp} (or V_{sp}–γ_{sp}) and (b) V_{sp}–h_R curves.

spanned the height. Very similar cracks appeared on both sides of the sample and covered the thickness of the wall. The peak load was attained at $V_{sp} = +28.9$ kN and -25.3 kN, with corresponding displacements $\delta_{sp} = +0.99$ mm and -1.25 mm (Fig. 8c,d), respectively.

Next, a noticeable stiffness drop occurred, and the cracking evolution proceeded asymmetrically. When loading in the positive direction, the damage was localised in the two vertical cracks at the ends, whereas a diagonal crack appeared when loading in the negative direction. The diagonal crack started from the top-right corner, where the damage was mainly focused. However, in both cases, the load decrease was quite gradual. A mixed failure mode (bending and shear) was activated. The near-collapse condition, in the two loading directions, was achieved at $\delta_{sp} = +6.71$ mm and -6.82 mm (Fig. 8e,f).

The hysteretic response of the shear load V_{sp} as a function of the distortion δ_{sp} (as well as the drift γ_{sp}) and horizontal displacement h_R of the right support is plotted in Fig. 10a,b. The former figure shows a gradual drop in stiffness after peak load, whereas the latter shows negligible horizontal displacements in the right support until the peak load was reached; then, sliding occurred as the spandrel was damaged and rotated, pulling the right pier away from the left one (the slip, always outward, reached a mean value of $h_R = +8.4$ mm at the near collapse condition). In addition, the residual slip in the complete

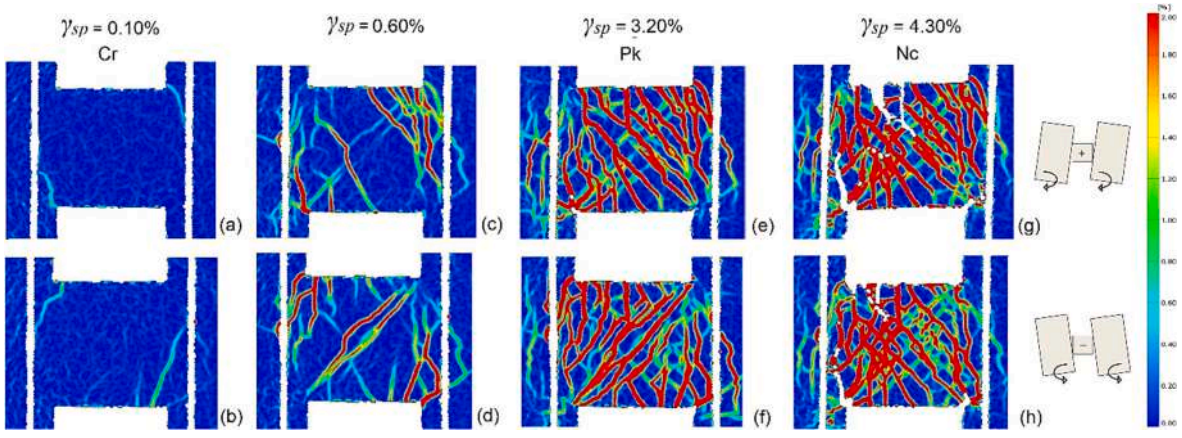

Fig. 12. Test S-R2-R1: cracks on the spandrel front side, detected by the DIC system (the gradient colour scale represents the tensile strains in the range of 0–2%).

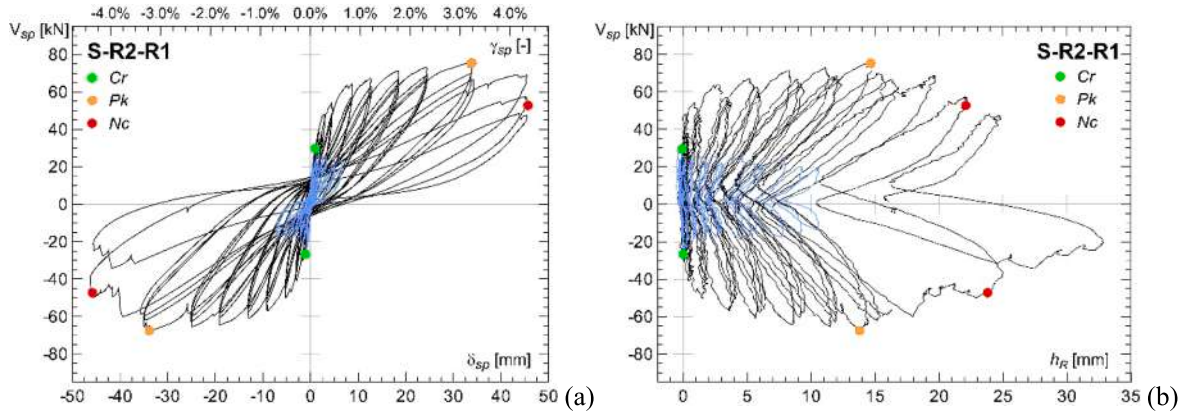

Fig. 13. Test S-R2-R1: (a) V_{sp}–δ_{sp} (or V_{sp}–γ_{sp}) and (b) V_{sp}-h_R curves. The curves of test S-R2-U1 are also reported in light blue for comparison. (For interpretation of the references to colour in this figure legend, the reader is referred to the web version of this article.)

unloading condition (V_{sp} = 0 kN) increased significantly with the number of load cycles.

In test S-R2-U2, the first cracks occurred at opposite corners at δ_{sp} = +0.74 mm (V_{sp} = +22.1 kN, Fig. 9a) and at δ_{sp} = − 0.49 mm (V_{sp} = − 22.4 kN, Fig. 9). The peak load was achieved quickly in both the positive (V_{sp} = +23.9 kN at δ_{sp} = +0.90 mm) and negative directions (V_{sp} = − 23.5 kN, at δ_{sp} = − 0.65 mm); then, the load decreased progressively in the post-peak cycles. The damage was located in two main, passing-through cracks at the spandrel extremities, with an almost vertical trend (Fig. 9c, d): the failure was governed by the bending mechanism; the distortion achieved at near collapse was about δ_{sp} = ±5.9 mm. As was the case for the previous sample, the V_{sp}–δ_{sp} (or V_{sp}–γ_{sp}) graph (Fig. 11a) shows a gradual but somewhat faster drop after peak load. The V_{sp}–h_R curve (Fig. 11b) again shows gradual separation between the piers after peak load (h_R = +7.2 mm at near collapse) and an increase in the residual slip.

4.2. Response of sample with coating on one side

Sample S-R2-U1 was repaired and strengthened with CRM coating on one side and then tested again after about six weeks. The evolution of the crack pattern is illustrated in Fig. 12, and the V_{sp}–δ_{sp} and V_{sp}–h_R curves are shown in Fig. 13.

The first cracking occurred at V_{sp} = +29.7 and − 26.7 kN at low spandrel distortions (δ_{sp} = +1.0 mm and − 1.1 mm, respectively) and involved just the mortar of the coating at the opposite corners of the spandrel (Fig. 12a,b). These cracks grew with a predominantly vertical trend, and parallel cracks formed in the vicinity. Inclined and diagonal cracks also occurred (Fig. 12c,d) and eventually spread over the entire surface of the coating. The peak resistance was reached at V_{sp} = +75.5 and − 67.5 kN (at δ_{sp} = ±33.8 mm), as shown in Fig. 12e,f. Then, the progressive failure of the GFRP wires occurred, resulting in a rapid load decrease leading to the near collapse condition. The vertical cracks were wider, and only the horizontal wires at the corners of the spandrel fractured (Fig. 14), denoting the final failure was in bending, although many inclined cracks were evident in the coating (Fig. 12g,h).

During the test, the bond between the coating and the wall was gradually lost over a large area of the spandrel; however, the coating remained effective because of the artificial diatons and GFRP connectors. No separation phenomena between the wall leaves were observed. On the back side (unstrengthened), the cracks in masonry (Fig. 15) were less widespread than the strengthened front side and tended to reproduce the pattern of the plain wall.

The V_{sp}–δ_{sp} (or V_{sp}–γ_{sp}) curve in Fig. 13a shows how stiffness gradually decreased after cracking; however, it was accompanied by hardening until peak resistance, which corresponds to the wire fractures. Once the wires fractured, total failure was imminent, as the sudden drop in resistance shows. The V_{sp}–h_R curve, plotted in Fig. 13b, indicates the right support slid in the very early stages (at a force of about ± 40 kN). The amount of sliding was about + 14.2 mm at peak load and + 23.0 mm at near collapse, with a residual sliding of + 10–15 mm when unloading.

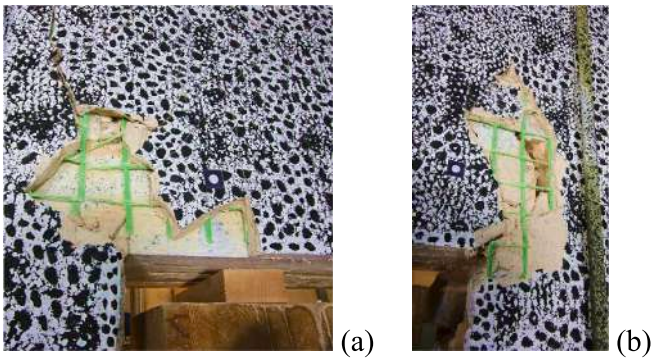

Fig. 14. S-R2-R1: details of the failure of some GFRP wires at the (a) left and (b) right lower corner of the spandrel (the coating was manually removed at the end of the test).

4.3. Response of sample with coating on both sides

Sample S-R2-U2 was repaired and strengthened by applying the coating to both sides. It was then tested after about six weeks. Fig. 16 reports the crack pattern evolution in the spandrel, while the V_{sp}–δ_{sp} and V_{sp}–h_R curves are plotted in Fig. 17.

Cracks originated at opposite spandrel corners with a vertical trend. This occurred at shear forces V_{sp} of + 48.6 kN and − 53.0 kN, and the corresponding spandrel distortions were + 2.06 mm and − 2.28 mm (Fig. 16a,b). The cracks progressively extended and, because of load reversal, eventually spanned across the entire height of the spandrel. From about V_{sp} = ±65 kN, uncontrolled unloading of the four jacks at the top of the sample occurred because of a malfunction of the pressure control system. With the reduced vertical load, a horizontal crack formed at the base of both piers, the interface of the masonry and the bottom RC beams: a crack opened below the left pier when loading in the positive direction (Fig. 18a), and the opposite occurred for the right pier (Fig. 18b). Each base crack opened from the inner corner of the pier across most of the width as a consequence of the pier rotation with respect to the lever beam, which originated from the pier's outer corner. The opening of the base crack limited the pier rotation, affecting the net spandrel distortion with respect to the values calculated through Eqs. (1) and (2). In this case, the estimation of the spandrel net distortion was

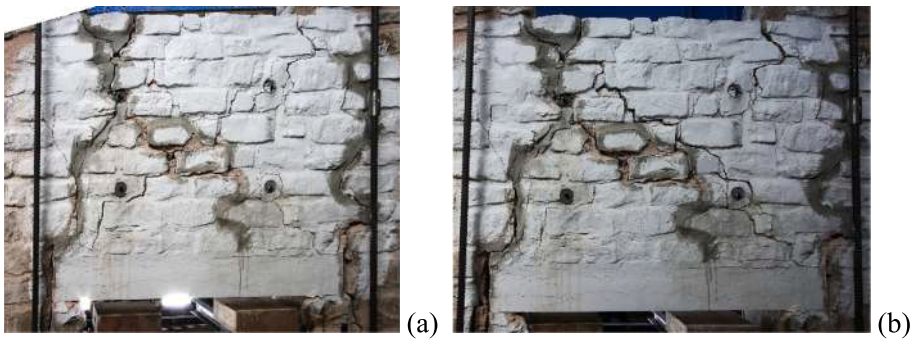

Fig. 15. S-R2-R1: cracks on the unstrengthened back face at near collapse for (a) positive and (b) negative loading directions.

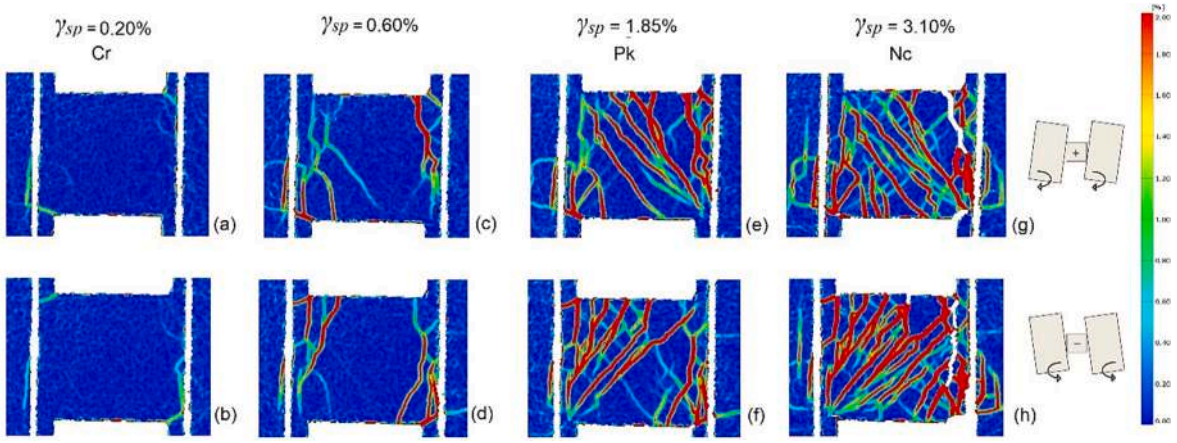

Fig. 16. S-R2-R2: cracks on the spandrel front side detected by the DIC system (the gradient colour scale represents the tensile strains in the range of 0–2%).

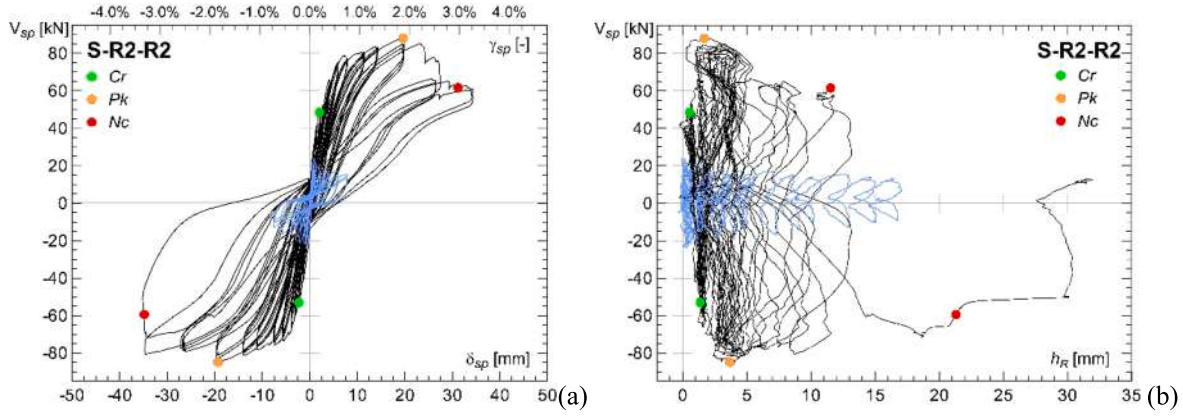

Fig. 17. Test S-R2-R2: (a) V_{sp}–δ_{sp} (or V_{sp}–γ_{sp}) and (b) V_{sp}–h_R curves. The curves of test S-R2-U2 are also reported in light blue for comparison. (For interpretation of the references to colour in this figure legend, the reader is referred to the web version of this article.)

possible using the DIC system, reading the actual piers rotations above the base cracks.

As the distortion continued, a few additional vertical cracks occurred near the spandrel ends (Fig. 16c,d); then, inclined cracks appeared in the coating within the spandrel area. The number of cracks gradually increased, covering the whole surface of the coating once the peak resistance was attained (V_{sp} = +88.1/−84.8 kN for δ_{sp} = +19.7/−19.3 mm; Fig. 16e,f). The collapse mode was flexural: in fact, with higher imposed rotations (Fig. 16 g,h), the vertical crack at the right side of the spandrel widened, and failures of the GFRP wires crossing the crack occurred at the front and back sides (Fig. 19). At the end of the test, debonding of the coating from the masonry was observed around the wider cracks. Furthermore, the initial separation of the wall leaves was detected in the pier portions below the lintel (Fig. 20).

The hysteretic response of the spandrel (Fig. 17a) resembles that of the specimen strengthened on only one side. However, the strength was greater in the case of the coating on both sides. The horizontal sliding at the right support (Fig. 17b) looked quite restricted until peak load (h_R < +4 mm); then, increasing values were recorded, also with a significant rate of residual deformation (>10 mm).

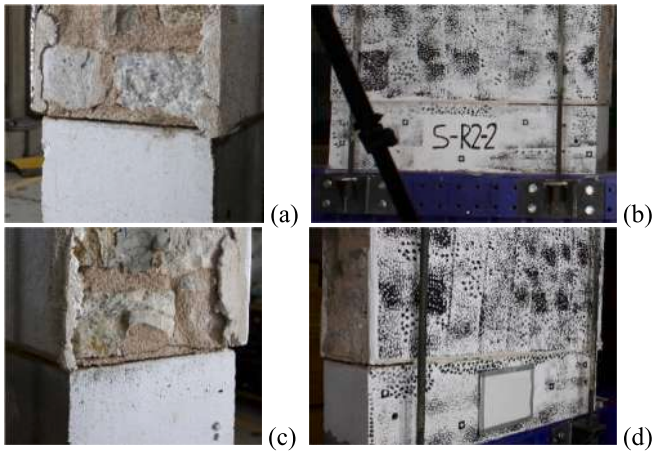

Fig. 18. S-R2-R2: details of the base cracks that occurred below the (a,b) left and (c,d) right pier in correspondence of δ_{sp} = (a) + 14 mm, (b) − 24.7 mm, (c) + 27 mm and (d) − 33 mm.

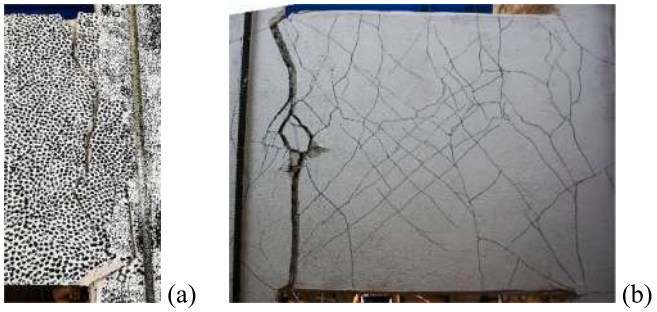

Fig. 19. S-R2-R2: details of the main crack at the spandrel right end at the end of the tests on (a) front and (b) back sides.

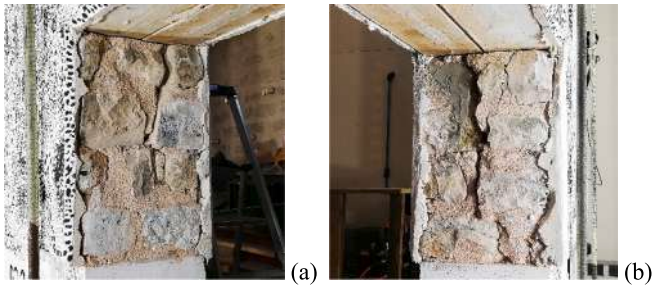

Fig. 20. S-R2-R2: local leaf separation at the (a) left and (b) right piers below the timber lintel at the end of the test.

5. Discussion

5.1. Resistance, displacement capacity and stiffness

The skeleton curves of the four samples are plotted for comparison in Fig. 21a. The values of shear force V_{sp}, distortion δ_{sp}, drift γ_{sp} and horizontal sliding of the right support h_R obtained from the four experimental tests are summarised in Table 4 for the three limit states of first cracking, peak load and near collapse (*Cr*, *Pk*, *Nc*, respectively). The main results in terms of peak load and ultimate drift are also compared in Fig. 21b-c.

The unstrengthened samples provided a mean resistance of 25.4 kN and a mean ultimate drift of 0.6 %. The single-sided coating led to a 2.8-fold increase in the spandrel resistance and 7.2 times the ultimate drift compared to the plain masonry. In the case of coating on both sides, corresponding improvements were by 3.4 and 5.2 times. Thus, both strengthening configurations were shown to be effective in increasing the spandrel in-plane performances, preventing occurrences of premature failures related to the debonding of the coating from the masonry and separation of wall leaves, which arose only in near collapse stages. Moreover, by comparing the two retrofitted configurations at peak load, the shear strength V_{sp} with the coating on both sides was only + 21 % higher than that of only one side; the ultimate drift was − 27 % lower. Of note, the performance of the specimen reinforced on both sides was compromised by the accidental loss of vertical stress in the piers, which led to opening of the cracks at the base of the piers and affected the boundary conditions of the spandrel. In fact, under the planned testing condition (presence of a constant axial stress in piers), the spandrel would behave roughly accordingly to a shear-type scheme. Due to loss of the axial stress in piers, spandrel ends were less rotationally constrained. Thus the actual static scheme would be in-between a shear-type and a cantilever configuration. It's reasonable to expect that, with a constant resistant bending moment, the resistance would be greater in the former case.

Regardless, the result of the test was interesting, demonstrating the effectiveness of the spandrel reinforcement in critical situations with the rocking of slender, weak piers.

The cycle stiffness K was evaluated as the slope of the peak-to-peak line within each loop of the V_{sp}–δ_{sp} curve, and the stiffness degradation is plotted in Fig. 22 as a function of δ_{sp} (or drift γ_{sp}). The initial stiffness in the unstrengthened and retrofitted sample was comparable (about 25–30 kN/mm); the stiffness decays then showed a power-law trend, with a softer degradation in the strengthened samples. The stiffness gap within the loops of a single target displacement was quite low and progressively reduced. At the end of the tests, the cycle stiffness degraded by about 90–95 % of the initial value.

5.2. Spandrels strains

The DIC system allowed to evaluate the trends of the equivalent horizontal strains at the top and the bottom of the spandrels (ε_{top} and ε_{bot}, respectively) and of the equivalent strains across the spandrels diagonals (ε_{d1} and ε_{d2}, respectively).

Strains ε_{top} and ε_{bot} were evaluated on a base length of about 1780 mm to also account for the cracks at the spandrel corners; ε_{d1} and ε_{d2} were evaluated on a base length of about 700 mm, avoiding the vertical cracks at the sides related to the bending mechanism but detecting diagonal strains within the central spandrel area. Diagonal *d1* lies in the direction connecting the left-bottom and the right-top spandrel corners, and *d2* goes from the left-top and the right-bottom corners.

Horizontal strains ε_{top} and ε_{bot} are plotted in Fig. 23, varying the shear force V_{sp}. In all the tests, the strains were positive (tensile strains), regardless of the loading direction, and consistent with the formation of the cracks. Moreover, non-negligible residual strains emerged after the occurrence of first cracking, when the samples were unloaded. The strains in sample S-R2-U2 were slightly higher than those in S-R2-U1, exhibiting a pure bending mechanism instead of the mixed failure mode (bending and shear) activated in the latter sample. The strengthened samples reached higher strains than the unstrengthened configurations, which is evident from their higher deformation capacity.

Strains ε_{top} and ε_{bot} were almost symmetrical in all samples, except for S-R2-R2, which is likely related to the alternate opening of cracks below the piers (as described in §4.3). In fact, since the pier with the open base crack had an effective rotation less than that of the other pier, higher ε_{top} than ε_{bot} was expected.

Diagonal strains ε_{d1} and ε_{d2} are plotted against the spandrel shear force V_{sp} in Fig. 24. Generally, the two diagonals tended to stretch alternatively (tensile strains) as the loading reversed and inclined cracks formed in the central area of the spandrel, while the compressive strains were negligible. For the positive loading direction, since the inclined

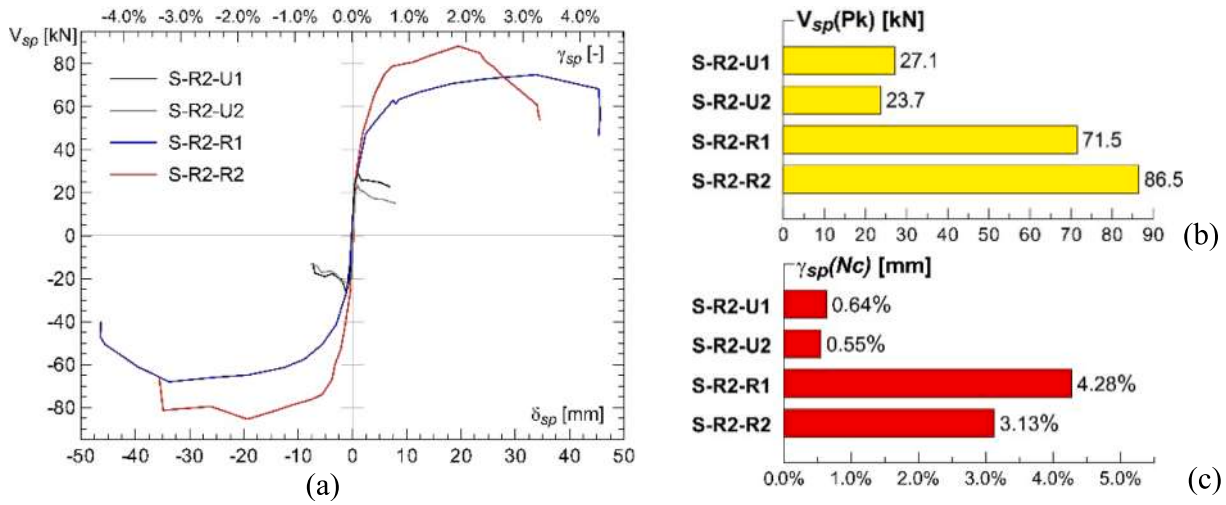

Fig. 21. Comparison among plain and retrofitted masonry samples in terms of (a) load-drift skeleton curves, (b) peak load and (c) ultimate drift.

Table 4
Values of the shear force V_{sp}, distortion δ_{sp}, corresponding drift γ_{sp} and horizontal sliding at the right support h_R measured in positive and negative loading directions for the first cracking, peak load and near collapse limit states.

	First cracking (*Fc*)				Peak load (*Pk*)				Near collapse (*Nc*)			
	V_{sp} [kN]	δ_{sp} [mm]	γ_{sp} [%]	h_R [mm]	V_{sp} [kN]	δ_{sp} [mm]	γ_{sp} [%]	h_R [mm]	V_{sp} [kN]	δ_{sp} [mm]	γ_{sp} [%]	h_R [mm]
S-R2-U1	23.3	0.58	0.054	0.00	28.9	0.99	0.094	0.00	20.2	6.71	0.633	9.20
	−24.0	−0.82	−0.077	0.00	−25.3	−1.25	−0.118	0.00	−17.7	−6.82	−0.643	7.60
S-R2-U2	22.1	0.74	0.069	0.00	23.9	0.90	0.085	0.00	16.7	5.98	0.564	7.10
	−22.4	−0.49	−0.04	0.00	−23.5	−0.65	−0.061	0.00	−16.4	−5.76	−0.543	7.20
S-R2-R1	29.7	1.00	0.094	−0.06	75.5	33.8	3.161	14.7	52.8	45.7	4.269	22.10
	−26.7	−1.11	−0.104	0.00	−67.5	−33.8	−3.162	13.8	−47.2	−45.8	−4.282	23.80
S-R2-R2	48.6	2.06	0.195	0.56	88.1	19.7	1.865	1.7	61.7	31.20	2.957	11.53
	−53.0	−2.28	−0.216	1.38	−84.8	−19.3	−1.827	3.7	−59.4	−34.80	−3.299	21.30

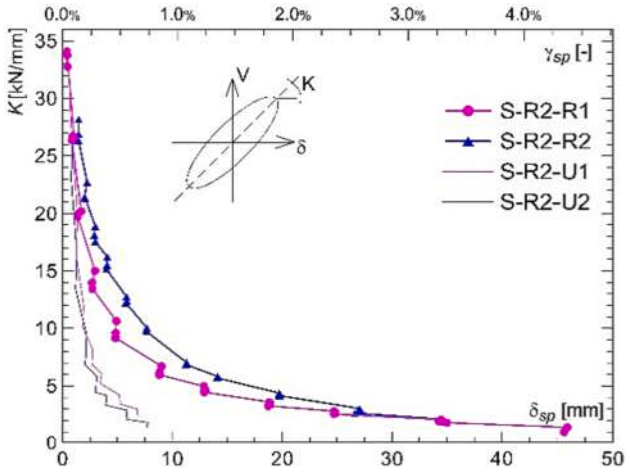

Fig. 22. Cycle stiffness by varying the target distortion δ_{sp} (or drift γ_{sp}).

cracks approximately follow the *d2* direction, ε_{d1} tended to increase while ε_{d2} was negligible. Differently, for the negative loading direction, the inclined cracks approximately follow the *d1* direction. Thus ε_{d2} tended to increase while ε_{d1} was negligible. In S-R2-U1, tensile strain ε_{d2} was higher than ε_{d1}, according to the asymmetric crack pattern (Fig. 8). Similar behaviour occurred in S-R2-U2 since ε_{d2} detected an inclined crack (Fig. 9); however, the strain values were lower than in S-R2-U1, which is consistent with a different failure mode. The tensile strains in the strengthened samples were larger because of the wider crack diffusion. Moreover, the strengthening on both sides in S-R2-R2, combined with the accidental base cracks, yielded lower diagonal strains compared to those in S-R2-R1.

5.3. Dissipative characteristics

To investigate the energy dissipation capacity, the cumulative input energy was compared with the dissipated hysteretic energy. The cumulative input energy E_{in} was calculated as the cumulative work needed to deform the spandrel from the beginning of the test to a specific value of distortion. For each loading cycle, it corresponds to the area under the positive and negative branches of the hysteretic loop, as shown in Fig. 25a. Similarly, the cumulative dissipated hysteretic energy E_{hys} was calculated as the sum of all the areas included in the hysteretic loops (Fig. 25b).

Table 5 presents the values of E_{in}, E_{hys} and E_{hys}/E_{in} at the reaching of the peak load (*Pk*) and the near collapse condition (*Nc*) in all the samples. In Fig. 26a,b, the total and dissipated cumulative energies are plotted as functions of the target displacement (i.e. spandrel distortion δ_{sp}). Three points for each target displacement are reported because of the three iterations. The plain samples (Fig. 26a) exhibited similar trends, whereas, in the case of strengthened samples, significantly higher input and dissipated cumulative energies were the result (Fig. 26b). Both E_{in} and E_{hys} were higher for S-R2-R2 than for S-R2-R1, but the ratio E_{hys}/E_{in} for $\delta_{sp} > 3$ mm was lower (Fig. 26c). For $\delta_{sp} > 8$–10 mm, the ratio tended to stabilise around 0.38 and 0.52 for S-R2-R2 and S-R2-R1. The tests on the two unstrengthened samples provided larger E_{hys}/E_{in} ratios (around 0.6–0.8, in accordance with the values previously obtained by Gattesco et al. [20]).

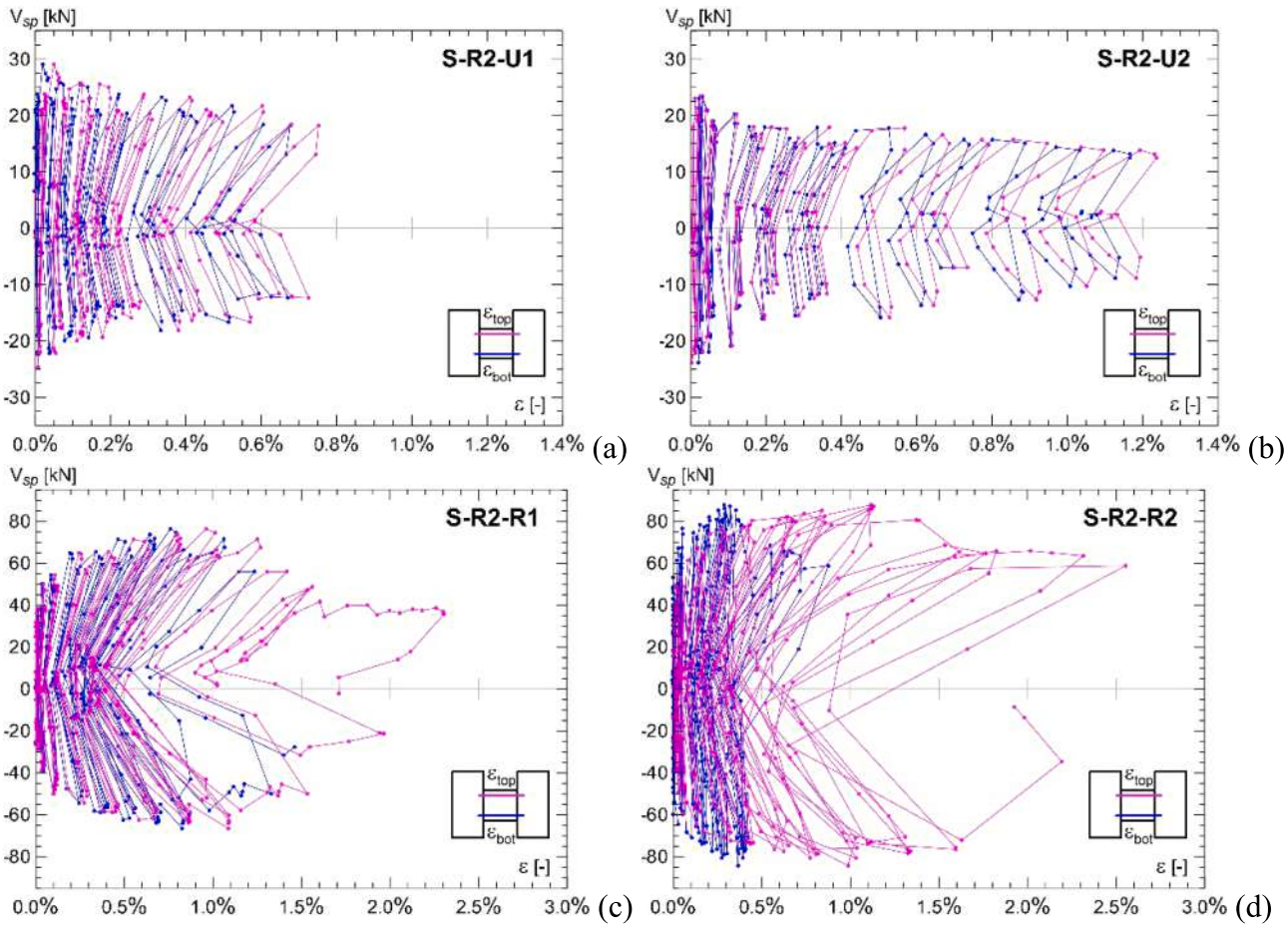

Fig. 23. Trends of the horizontal strains at the top (ε_{top}) and bottom (ε_{bot}) of the spandrels monitored by the DIC system as functions of shear force V_{sp}.

An approximate value of the equivalent hysteretic damping of the samples was determined using the equation provided by Chopra [35] and FEMA 440 [36]:

$$\xi_{hys} = \frac{E_{hys,i}}{2\pi E_{S0,i}} \tag{3}$$

where $E_{hys,i}$ is the hysteresis energy dissipated within each cycle and $E_{S0,i}$ is the strain energy associated with the cycle stiffness in each cycle, as illustrated in Fig. 25c.

In the unstrengthened samples, mean values of ξ_{hys} were about 0.15 for large damage (Table 5). The trends of ξ_{hys} of the strengthened samples are reported in Fig. 26d, again distinguishing values for each of the three load iterations. The difference in ξ_{hys} was generally more evident between the first and second cycles than between the second and third. Additionally, this difference tended to decrease as δ_{sp} increased. Approaching the peak load condition, ξ_{hys} was similar in all cycles at about 0.11 in S-R2-R1 and 0.08 in S-R2-R2. At the near-collapse limit, ξ_{hys} was about 0.14 and 0.09 for walls S-R2-R1 and S-R2-R2, respectively. Therefore, the spandrels with coating on one side performed slightly better in terms of ξ_{hys}. This result agrees with the crack pattern in the mortar coating, as it was slightly more diffused in S-R2-R1 (Fig. 13). The cracking at the base of S-R2-R2 (§4.3) likely affected the results. The values obtained for S-R2-R1 are very close to those obtained by Boem and Gattesco [37] for masonry barrel vaults strengthened at the extrados or at the intrados with the CRM technique.

6. Conclusions

The effectiveness of the CRM applied on one or both wall faces as a technique for the seismic strengthening of historical rubble stone masonry spandrels was assessed experimentally. Quasi-static cyclic tests were carried out on full-scale, H-shaped masonry panels in a setup with controlled rotations of piers and direct measurements of shear force.

The unstrengthened samples performed quite similarly in terms of peak resistance (V_{sp} = 25.4 kN), ultimate drift (γ_{sp} = 0.60 %) and cumulative dissipated energy (E_{hys} = 0.72 kJ) at the near collapse condition). The crack pattern was characterised by a few wide cracks located mostly at the spandrels' extremities or along the diagonals, which were related to the activation of bending or diagonal cracking mechanisms, respectively. In contrast, the strengthened samples developed a very diffuse damage pattern in the mortar coating, with many thin cracks covering most of the spandrel area and large, observable sample deformations before collapse, which were due to GFRP wires fracturing. As a result, the performances of the strengthened samples demonstrated the effectiveness of the intervention, which increased the peak resistance by 2.8 and 3.4 times that of the plain condition for the case of coating on one or two sides, respectively. Furthermore, the strengthening provided considerable additional ductility, displacement capacity and energy dissipation, with ultimate drifts more than five times greater and dissipated energy more than thirty times larger.

The behaviour of the spandrel with coating on only one side was particularly significant because, different from previous findings (§1), no eccentric phenomena related to the asymmetrical stiffness occurred. This is because the boundary conditions in these tests (continuity with the lateral piers) were much more realistic than those of the isolated panels investigated in the literature. Finally, the low–medium axial stress level in the panels (more consistent with actual configurations) mitigated this occurrence.

The tests demonstrate that effective connections among the masonry leaves and between the reinforced mortar coating and masonry are

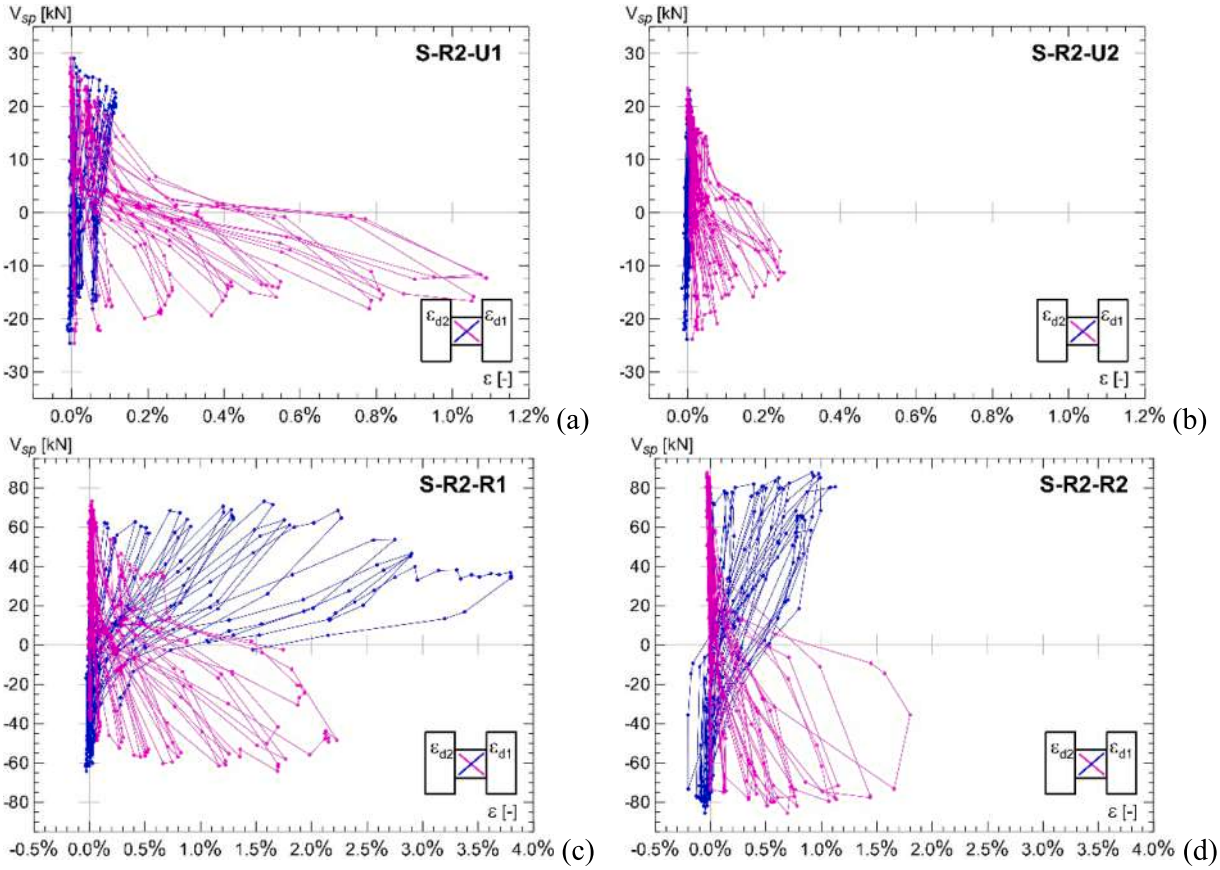

Fig. 24. Trends of the diagonal strains of the spandrels (ε_{d1} and ε_{d2}) monitored by the DIC system, varying the shear force V_{sp}.

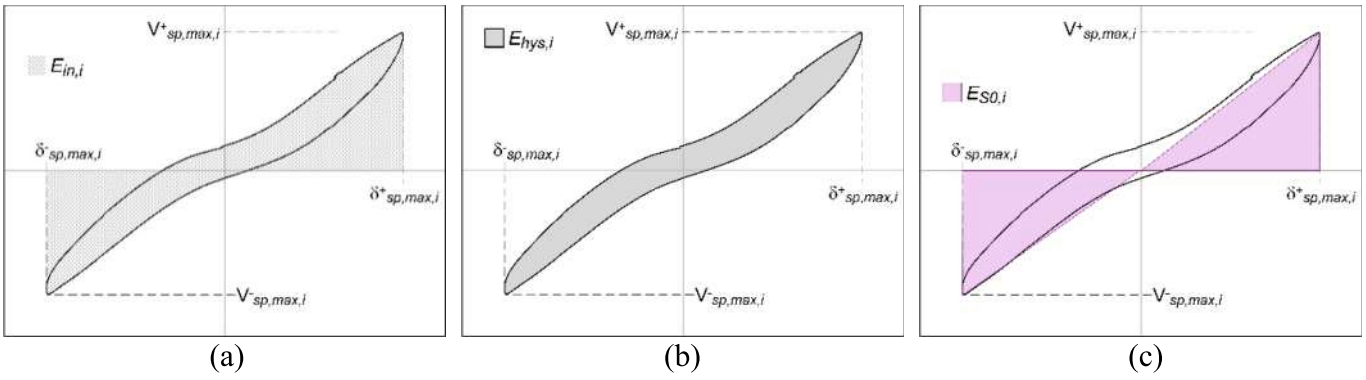

Fig. 25. Schematisation of input energy and dissipated hysteretic energy in the i^{th} loading cycle.

Table 5
Values of cumulative input energy E_{in} and dissipated hysteresis E_{hys} at resistance peak (*Pk*) and at near collapse (*Nc*), mean cumulative energy ratio in the cycles (E_{hys}/E_{in}).

	E_{in} [J]		E_{hys} [J]		E_{hys}/E_{tot} [-]		ξ_{hys} [-]	
	Pk	*Nc*	*Pk*	*Nc*	*Pk*	*Nc*	*Pk*	*Nc*
S-R2-U1	119.8	1233.0	78.6	807.8	0.66	0.66	–	0.12
S-R2-U2	34.9	831.2	23.5	641.1	0.67	0.77	–	0.17
S-R2-R1	18496.4	30045.2	9462.8	16591.2	0.51	0.55	0.11	0.14
S-R2-R2	16100.1	35706.6	5941.8	1436.2	0.37	0.40	0.08	0.09

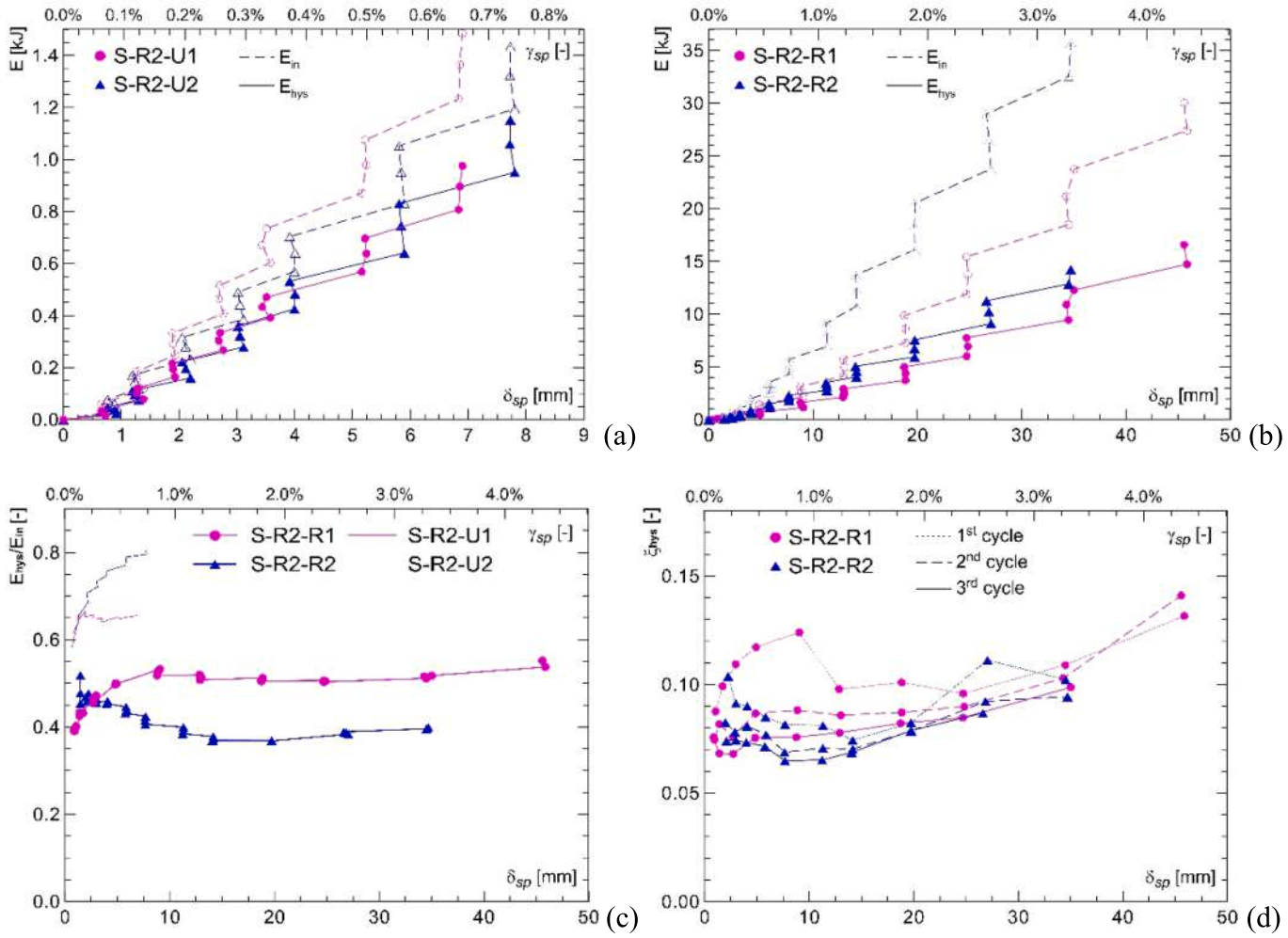

Fig. 26. Energy dissipation as a function of the target distortion δ_{sp} (or drift γ_{sp}): (a,b) cumulative dissipated E_{hys} and total E_{hys}, (c) E_{hys}/E_{hys} ratio and (d) equivalent hysteretic damping ξ_{hys} at each cycle of the retrofitted samples.

essential to prevent premature layers separation and debonding. These detailed aspects must be properly addressed by the professionals in the design and application phases; otherwise, the intervention's effectiveness can be compromised. The transverse connectors introduced in the tested samples performed effectively against this occurrence.

Additional spandrel tests are in progress on various masonry types (solid brick masonry, in single and double leaves) to extend the experimental database. The test results presented in this paper will be useful for the validation of advanced numerical models aimed at the in-depth parametric study of the performances of strengthened spandrels with varying geometry and materials. This work will define simplified but reliable analytical correlations to describe the spandrel behaviour, which can be used in the simplified global analysis of entire CRM-strengthened structures.

One of the authors, Eng. Allen Dudine, is a collaborator of Fibre Net s.p.a., which manufactures products related to the research described in this paper. However, Eng. Allen Dudine had no influence over the data collection, analysis or interpretation. The other authors declare no conflicts of interest.

CRediT authorship contribution statement

N. Gattesco: Conceptualization, Methodology, Investigation, Writing – review & editing, Supervision, Project administration, Funding acquisition. **I. Boem:** Conceptualization, Methodology, Data curation, Writing – original draft, Writing – review & editing, Visualization. **E. Rizzi:** Investigation, Data curation, Writing – review & editing. **A. Dudine:** Investigation, Resources. **M. Gams:** Conceptualization, Methodology, Investigation, Resources, Data curation, Writing – review & editing.

Declaration of Competing Interest

The authors declare that they have no known competing financial interests or personal relationships that could have appeared to influence the work reported in this paper.

Data availability

Data will be made available on request.

Acknowledgements

This work was supported by the project CONSTRAIN, funded by the Interreg Italy-Slovenia Cooperation Program 2014–2020 and led by the University of Trieste (Italy) with the University of Ljubljana (Slovenija) and FibreNet S.p.A., Igmat d.d., Veneziana Restauri Costruzioni S.r.l. and Kolektor CPG d.o.o.

The support of the Italian Department of Civil Protection (Reluis 2022–2024, WP5) and the Slovenian Research Agency (project P2-0185) is also gratefully acknowledged.

References

[1] Sorrentino L, Cattari S, da Porto F, Magenes G, Penna A. Seismic behaviour of ordinary masonry buildings during the 2016 central Italy earthquakes. Bull Earthquake Eng 2019;17(10):5583–607.

[2] Gautam D, Chettri N, Tempa K, Rodrigues H, Rupakhety R. Seismic vulnerability of bhutanese vernacular stone masonry buildings: from damage observation to fragility analysis. Soil Dyn Earthq Eng 2022;160:107351. https://doi.org/10.1016/j.soildyn.2022.107351.

[3] Bayraktar A, Coşkun N, Yalçin A. Performance of masonry stone buildings during the March 25 and 28, 2004 Aşkale (Erzurum) earthquakes in Turkey. J Perform Constr Fac 2007;21(6):432–40. https://doi.org/10.1061/(ASCE)0887-3828(2007)21:6(432).

[4] Grünthal G Ed. European Macroseismic Scale 1998 (EMS-98), Cahiers du Centre Européen de Géodynamique et de Séismologie, 15, Luxembourg: Centre Européen de Géodynamique et de Séismologie.

[5] Borri A, Corradi M, De Maria A. The failure of masonry walls by disaggregation and the Masonry Quality Index. Herit 2020;3(4):1162–98. https://doi.org/10.3390/heritage3040065.

[6] Saretta Y, Sbrogiò L, Valluzzi MR. Seismic response of masonry buildings in historical centres struck by the 2016 Central Italy earthquake. Calibration of a vulnerability model for strengthened conditions. Constr Build Mater 2021;299:123911. https://doi.org/10.1016/j.conbuildmat.2021.123911.

[7] Sisti R, Di Ludovico M, Borri A, Prota A. Seismic performance of strengthened masonry structures: actual behaviour of buildings in Norcia and Campi Alto during the 2016 Central Italy seismic sequence. Bull Earthquake Eng 2022;20:321–48. https://doi.org/10.1007/s10518-021-01248-0.

[8] https://www.ita-slo.eu/en/constrain (accessed Jun. 10, 2023).

[9] Gattesco N, Boem I, Rizzi E, Bez A, Gams M, Farič M, Pučnik V, Dudine A. The Experimental Campaign and Numerical Simulations of the CONSTRAIN Project. Technical report, 2022. Standard project co-fincanced by the European Regional Development Fund.

[10] Gattesco N, Boem I. Characterization tests of GFRM coating as a strengthening technique for masonry buildings. Compos Struct 2017;165:209–22. https://doi.org/10.1016/j.compstruct.2017.01.043.

[11] Gattesco N, Boem I. Experimental and analytical study to evaluate the effectiveness of an in-plane reinforcement for masonry walls using GFRP meshes. Constr Build Mater 2015;88:94–104. https://doi.org/10.1016/j.conbuildmat.2015.04.014.

[12] Gattesco N, Boem I. Out-of-plane behavior of reinforced masonry walls: Experimental and numerical study. Compos B Eng 2017;128:39–52. https://doi.org/10.1016/j.compositesb.2017.07.006.

[13] Padalu PKVR, Singh Y, Das S. Efficacy of basalt fibre reinforced cement mortar composite for out-of-plane strengthening of unreinforced masonry. Constr Build Mater 2018;191:1172–90. https://doi.org/10.1016/j.conbuildmat.2018.10.077.

[14] D'Antino T, Carozzi FG, Poggi C. Diagonal shear behavior of historic walls strengthened with composite reinforced mortar (CRM). Mater Struct 2019;52:114. https://doi.org/10.1617/s11527-019-1414-1.

[15] Del Zoppo M, Di Ludovico M, Balsamo A, Prota A. In-plane shear capacity of tuff masonry walls with traditional and innovative Composite Reinforced Mortars (CRM). Constr Build Mater 2019;210:289–300. https://doi.org/10.1016/j.compositesb.2019.04.020.

[16] Donnini J, Maracchini G, Lenci S, Corinaldesi V, Quagliarini E. TRM reinforced tuff and fired clay brick masonry: experimental and analytical investigation on their in-plane and out-of-plane behavior. Constr Build Mater 2021;272:121643. https://doi.org/10.1016/j.conbuildmat.2020.121643.

[17] Tomaževic M. Earthquake-resistant Design of Masonry Buildings, Series on Innovation in Structures and Construction. Imperial College Press: London, UK, 1999.

[18] Augenti N, Parisi F, Prota A, Manfredi G. In-plane lateral response of a full-scale masonry subassemblage with and without an inorganic matrix–grid strengthening system. J Compos Constr 2011;15:578–90. https://doi.org/10.1061/(ASCE)CC.1943-5614.0000193.

[19] Ismail N, Ingham JM. In-plane and out-of-plane testing of unreinforced masonry walls strengthened using polymer textile reinforced mortar. Eng Struct 2016;118:167–77. https://doi.org/10.1016/j.engstruct.2016.03.041.

[20] Gattesco N, Macorini L, Dudine A. Experimental response of brick-masonry spandrels under in-plane cyclic loading. J Struct Eng 2016;142:04015146. https://doi.org/10.1061/(ASCE)ST.1943-541X.0001418.

[21] Beyer K, Dazio A. Quasi-static cyclic tests on masonry spandrels. Earthq Spectra 2012, 28(3), 907–929. DOI: doi:10.1193/1.4000063.

[22] Basili M, Vestroni F, Marcari G. Brick masonry panels strengthened with textile reinforced mortar: experimentation and numerical analysis. Constr Build Mater 2019;227:117061. https://doi.org/10.1016/j.conbuildmat.2019.117061.

[23] Marcari G, Basili M, Vestroni F. Experimental investigation of tuff masonry panels reinforced with surface bonded basalt textile-reinforced mortar. Compos B Eng 2017;108:131–42. https://doi.org/10.1016/j.compositesb.2016.09.094.

[24] Parisi F, Iovinella I, Balsamo A, Augenti N, Prota A. In-plane behaviour of tuff masonry strengthened with inorganic matrix–grid composites. Compos B Eng 2013;45(1):1657–66. https://doi.org/10.1016/j.compositesb.2012.09.068. 23.

[25] Casacci S, Gentilini C, Di Tommaso A, Oliveira DV. Shear strengthening of masonry wallettes resorting to structural repointing and FRCM composites. Constr Build Mater 2019;206:19–34. https://doi.org/10.1016/j.conbuildmat.2019.02.044.

[26] Gattesco N, Amadio C, Bedon C. Experimental and numerical study on the shear behavior of stone masonry walls strengthened with GFRP reinforced mortar coating and steel-cord reinforced repointing. Eng Struct 2015;90:143–57. https://doi.org/10.1016/j.engstruct.2015.02.024.

[27] Tomaževič M, Gams M, Berset T. Strengthening of stone masonry walls with composite reinforced coatings. Bull Earthquake Eng 2015;13(7):2003–27. https://doi.org/10.1007/s10518-014-9697-7.

[28] Castori G., Borri A, Corradi M, Righetti L. Structural analysis of transversal steel connectors applied on multi-leaf walls. In: Proceedings of the 13th Canadian Masonry Symposium, 4-7 June 2017, Halifax, Canada.

[29] Roselli G, Mirabile Gattia D, AlShawa O, Cinaglia P, Di Girolami G, Francola C, et al. Mortar analysis of historical buildings damaged by recent earthquakes in Italy. Eur Phys J Plus 2019;134:540. https://doi.org/10.1140/epjp/i2019-13024-2.

[30] EN 1015-11:2019. Methods of test for mortar for masonry – Part 11: Determination of flexural and compressive strength of hardened mortar. Brussels: CEN, 2019.

[31] EN 1052-1:1998. Methods of test for masonry – Part 1: Determination of compressive strength. Brussels: Comité Européen de Normalisation – CEN, 1998.

[32] ISO 10406-1:2015. Fibre-reinforced polymer (FRP) reinforcement of concrete – Test methods – Part 1: FRP bars and grids. International Organization for Standardization – ISO, 2015.

[33] Oats RC, Dai Q, Head M. Digital Image Correlation advances in structural evaluation applications: A review. Pract Period Struct Des Constr 2022;27(4):03122007. https://doi.org/10.1061/(ASCE)SC.1943-5576.0000725.

[34] Howlader MK, Masia MJ, Griffith MC. Digital image correlation for the analysis of in-plane tested unreinforced masonry walls. Struct 2021;29:427–45. https://doi.org/10.1016/j.istruc.2020.11.051.

[35] Chopra AK. Dynamics of structures: theory and applications to earthquake engineering. Englewood Cliffs, NJ: Prentice-Hall, 1995.

[36] FEMA440. Improvement of nonlinear static seismic analysis procedures, Washington, D.C: Federal Emergency Management Agency – FEMA, 2005.

[37] Boem I, Gattesco N. Cyclic behavior of masonry barrel vaults strengthened through Composite Reinforced Mortar, considering the role of the connection with the abutments. Eng Struct 2021;228:111518.